Chapter 8
Semi-adiabatic Temperature Rise and Thermal Cracking Prediction for Mass Concrete

8.1 General

Even though the proposed model by Saengsoy (2002) is satisfactory for predicting the adiabatic temperature of the test results, but in the real situation of mass concrete, the semi-adiabatic temperature rise is observed due to heat loss to environment. Flow chart of the proposed model for simulating thermal cracking of mass concrete is shown in Fig. 8.1. The input values are the same as those of Saengsoy (2002). However, the dimension, environmental and boundary conditions must be input in the proposed model as well. In this study, the proposed model is not only aimed to predict the semi-adiabatic temperature of mass concrete but also to predict the risk of cracking that may happen due to restraint of concrete. Heat of hydration and pozzolanic reaction which were obtained from the modified adiabatic temperature rise model were used as the input for a commercial FEM program (MARC). Thermal properties such as specific heat, thermal conductivity and coefficient of thermal expansion are obtained from the proposed thermal properties model as mentioned in chapters 5, 6 and 7. FEM program was used to analyze the semi-adiabatic temperature and restrained strain of concrete. For the proposed model, three dimensional eight node brick were used in the analysis. The considered time interval is divided into several increments and one increment is equal to one hour. The couple thermo-mechanical problem was used in the analysis in which thermal analysis is solved first. The temperature obtained from the thermal analysis is used as the input for the computation of the restrained strain. Tensile strain capacity (TSC) of concrete is used as the criterion to evaluate the risk of thermal cracking in mass concrete (Lu et al., 2001; Tongarronsri and Tangtermsirikul, 2008). TSC of concrete used in this study was obtained from the test results conducted by Lu et al. (2001) as well as Tongarronsri and Tangtermsirikul (2008). The method of the analysis is described in this chapter.

8.2 Heat Transfer Analysis

By the use of the common heat transfer analysis, which was mentioned by many researchers (Kwak et al., 2006; Sarker et al., 1999; Maekawa et al., 1999; Wang and Dilger, 1995), with the heat of hydration and pozzolanic reaction and thermal properties, the semi-adiabatic temperature distribution in the mass concrete can be analyzed. The governing equation of three dimensional heat transfer for temperature prediction of mass concrete with consideration of heat of hydration is shown in Eq. (8.1).

$$\rho c \frac{\partial T}{\partial t} = q_{hy} + \frac{\partial}{\partial x}\left(k_x \frac{\partial T}{\partial x}\right) + \frac{\partial}{\partial y}\left(k_y \frac{\partial T}{\partial y}\right) + \frac{\partial}{\partial z}\left(k_z \frac{\partial T}{\partial z}\right) \tag{8.1}$$

where: k_x, k_y, k_z are the thermal conductivity of concrete in x, y and z direction, respecitvely (kcal/m hr ^oC). ρ is concrete density (kg/m^3), c is specific heat of concrete (kcal/ kg ^oC), q_{hy} is the rate of internal heat generated by hydration and pozzolanic reaction per unit volume (kcal/m^3 hr). t is age of concrete (hr.). T is temperature of concrete (^oC).

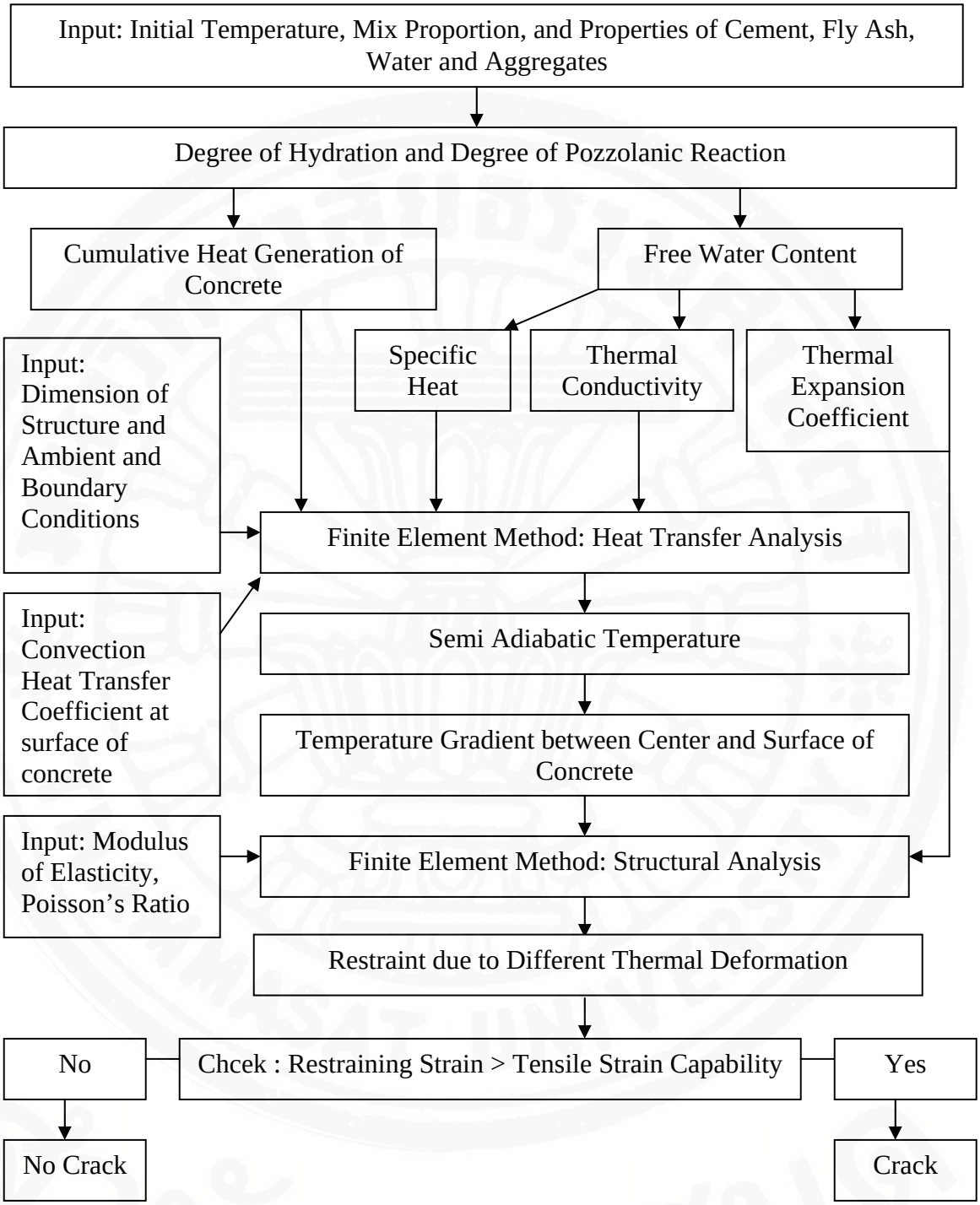

Fig 8.1 Flow chart of the proposed model for simulating thermal cracking of mass concrete

The total heat generation of concrete was computed from the summation of the heat liberated due to the reaction of each cement compounds including the formation of ettringite and monosulphate and the reaction of fly ash as mentioned in Chapter 3. The initial condition is the initial temperature of concrete at the time just after mixing (t = 0 day).

The heat transfer inside the concrete mass is governed by Eq. (8.1), however, the condition at the concrete surface is different. Fig. 8.2 shows the behaviors of heat transfer in mass concrete. The conduction process plays an important role in transferring heat within the interior elements. However, for exterior elements, the conduction play a dominant role in transferring heat within concrete while the presence of wind and solar radiation affect the temperature profile significantly and must be considered. The net heat flow on concrete surface can be calculated as shown in Eq. (8.2).

$$q = q_s - q_c - q_r \tag{8.2}$$

where: q is the net heat flow on a concrete surface, q_s is the total radiation absorbed, q_r is the re-radiation by concrete and q_c is the heat loss by the convection.

The heat transfer at the surface of mass concrete must include the effect of the presence of wind and solar radiation. The convective heat transfer play a dominant role in transferring heat between surface of mass concrete and environment (between concrete and air). The amount of heat transfer at the surface of concrete can be calculated according to the Newton's cooling law. For simplicity, the radiation is usually accounted together with convection, through a single convection-radiation coefficient (Faria et al., 2006). The convective heat transfer at concrete surface can be expressed as

$$q_c = h(T_s - T_a) \tag{8.3}$$

where q_c is the convective heat flux per unit area, h is the combined convection-radiation heat transfer coefficients (kcal/m^2 hr ^{o}C), T_s and T_a are the surface and air temperature.

In the simulation of the experiment conducted in the lab, concretes were cast in formworks and all surfaces were exposed to the air, as a result, the heat loss to the surrounding is by convection process. So, the convection process can be determined for calculating the heat transfer to the surrounding from all surfaces of concrete. In the real mass concrete footing, loss to surrounding air is also processed by convection. Normally, the side and bottom surfaces of a footing are covered by subsoil and heat dissipates from concrete to the surrounding soil by conduction process. However, the problem can be simplified by the assumption that the amount of heat loss to the surrounding subsoil is assumed to be done by the convection process. In other word, amount of heat loss to surrounding subsoil by conduction is quantified to be the same as convection. This kind of assumption and boundary condition was used in previous study of other researchers (Faria et al., 2006). The finite element mesh is shown in Fig 8.3.

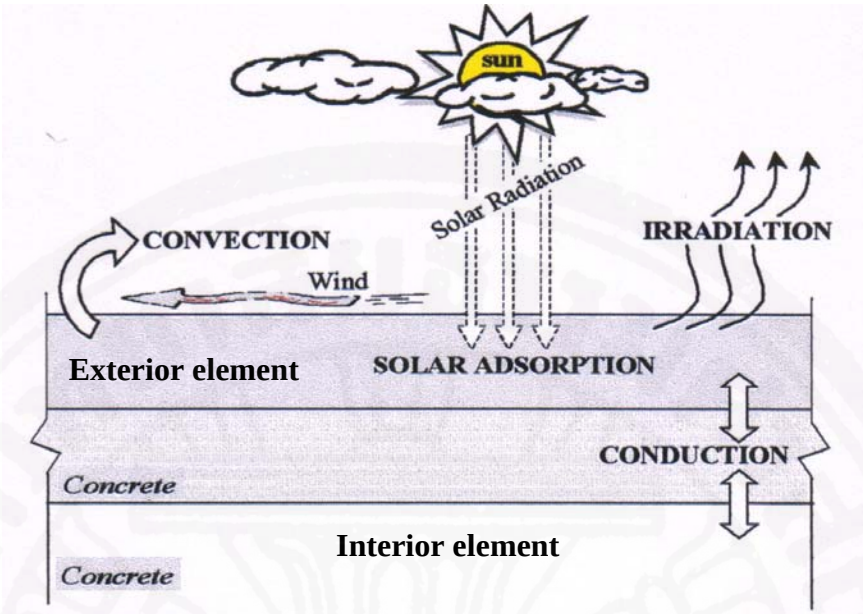

Fig. 8.2 Behaviors of heat transfer of mass concrete (Figure from Ruiz et al., 2001)

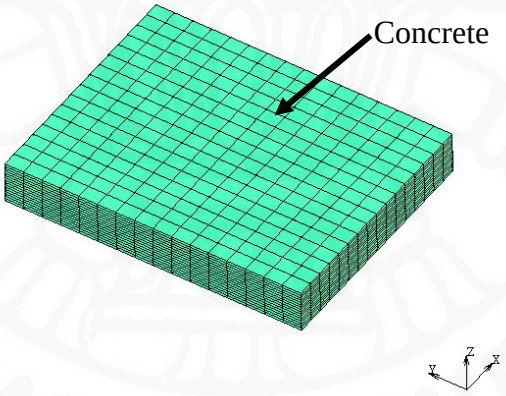

Fig. 8.3 Finite element mesh of a footing

8.3 Verification of the Proposed Semi-adiabatic Temperature Rise Model

8.3.1 Verification with the test results conducted in the lab

The experiments conducted by previous researchers (Sarker et al., 1999; Mony, 1999; Tatsanagoson, 1999) were used in the verification. Concrete specimens were cast in the insulated foam-plywood boxes. Thermocouples were placed at the center to measure the temperature. Data logger was used to record the temperature history throughout the test period. The details of the test samples are shown in Appendix D. Table D1 shows the mix proportion of the specimens. The size of the specimens, thickness of foam and plywood are shown in Table D2. Physical properties and chemical composition of the tested cement and

fly ash are shown in Table D3 and D4, respectively. The setup of specimens is shown in Fig. 8.4. Two types of fly ash with different CaO content were used. The comparison between the measured and predicted temperature at the center of specimens are shown in Figs 8.5 to 8.15. Figs 8.5 to 8.9show the results of the mixes without fly ash while Figs 8.10 to 8.12 and Figs 8.13 to 8.15 show the results of the mixes with fly ash types A and B (FAA and FAB). The verifications show that the model is satisfactory for predicting temperature of the test results.

Fig 8.4 Testing of semi-adiabatic temperature of concrete

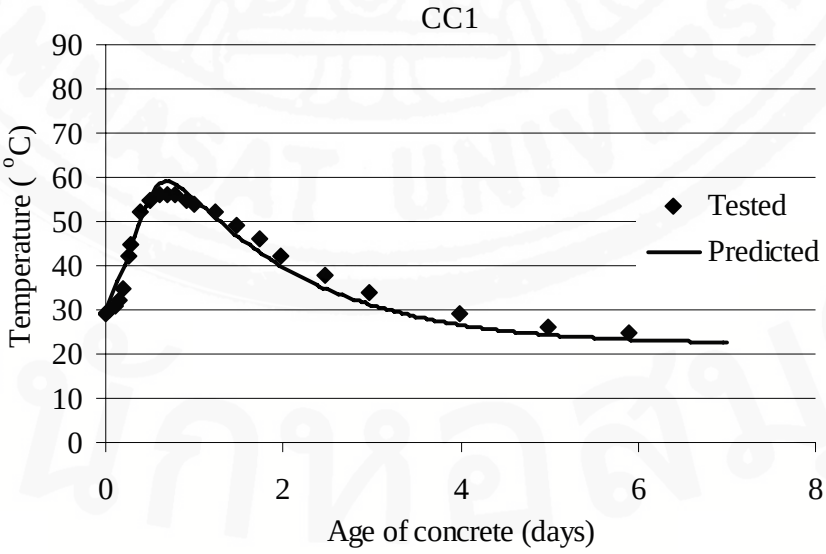

Fig. 8.5 Comparison between test and predicted temperature of Portland cement mixture (CC1)

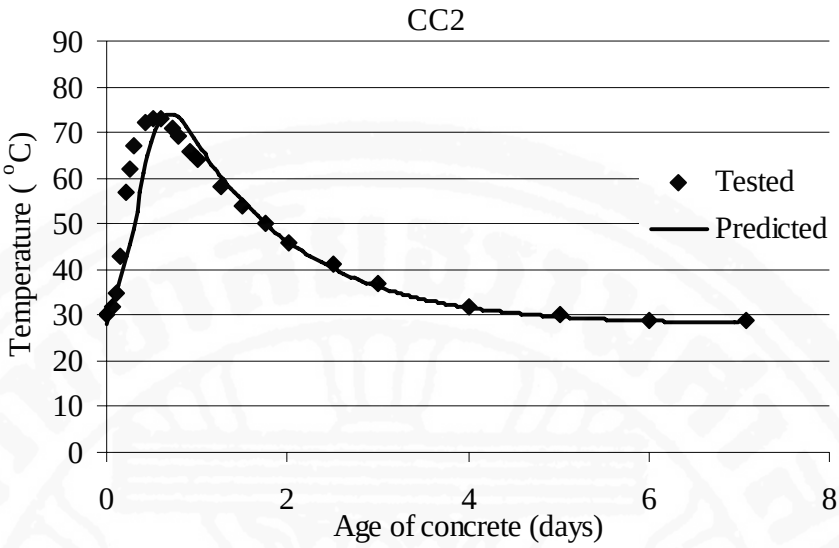

Fig. 8.6 Comparison between test and predicted temperature of Portland cement mixture (CC2)

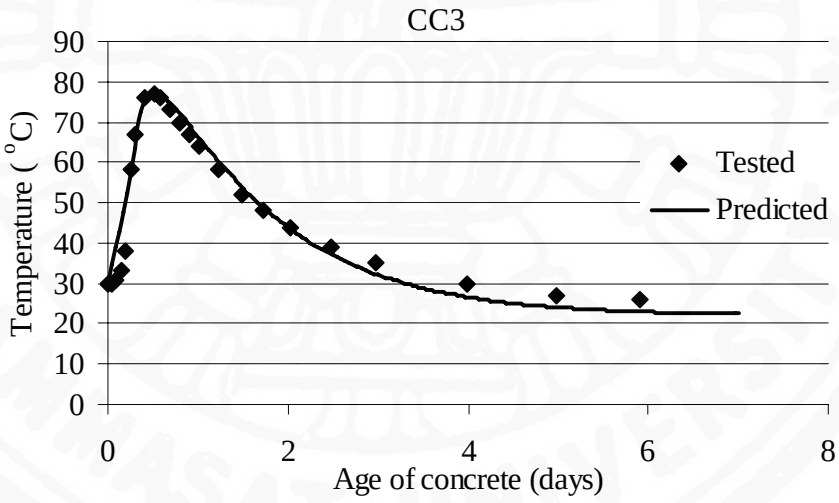

Fig. 8.7 Comparison between test and predicted temperature of Portland cement mixture (CC3)

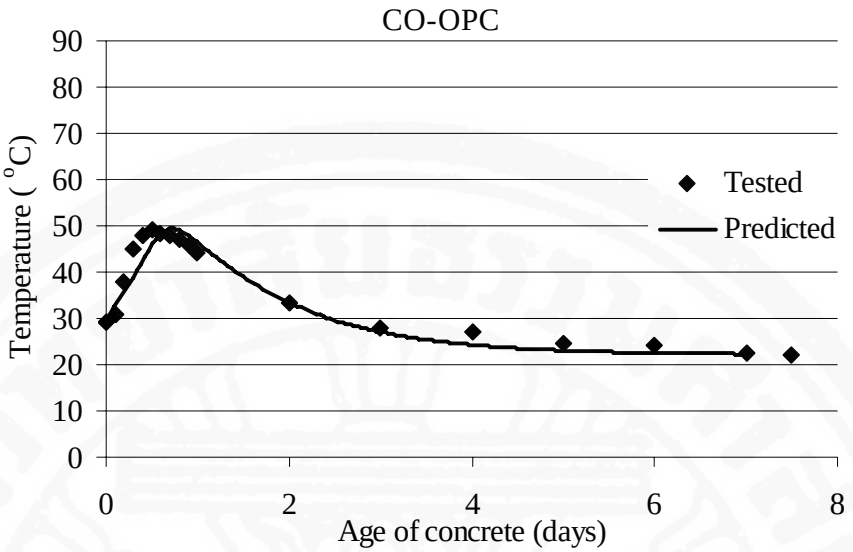

Fig. 8.8 Comparison between test and predicted temperature of Portland cement mixture (CO-OPC)

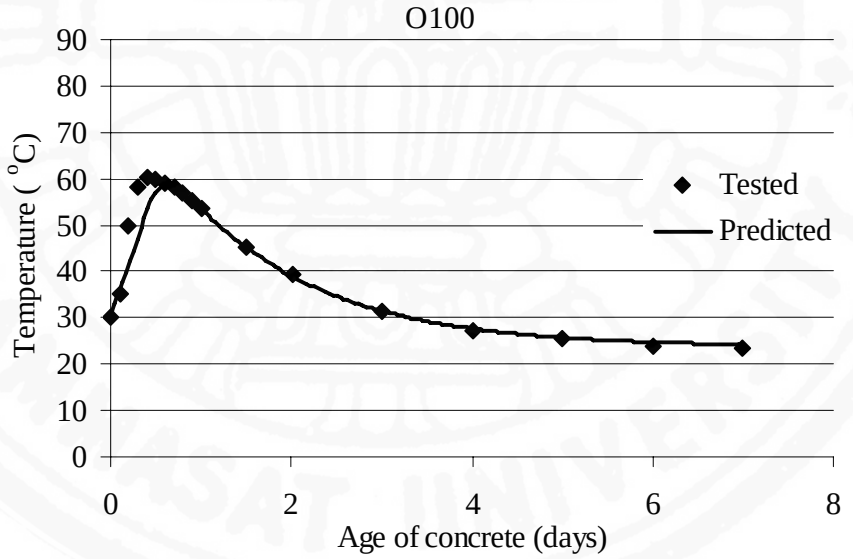

Fig. 8.9 Comparison between test and predicted temperature of Portland cement mixture (O100)

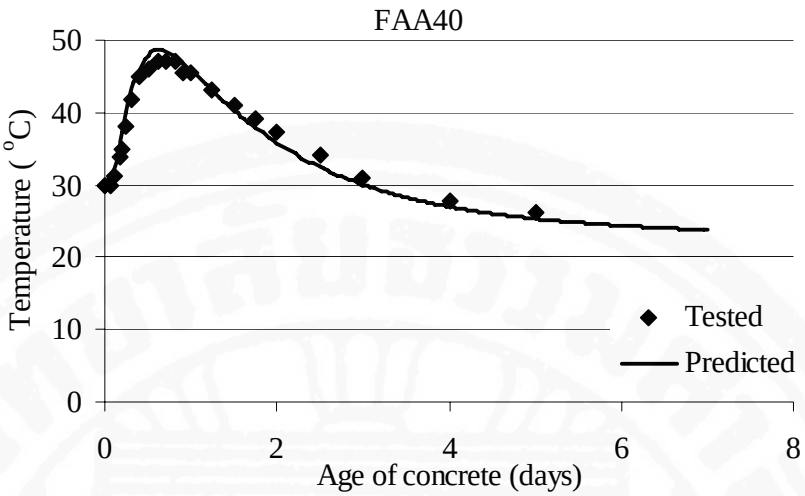

Fig. 8.10 Comparison between test and predicted temperature of blended cement mixture with 40% replacement of fly ash type A (FAA40)

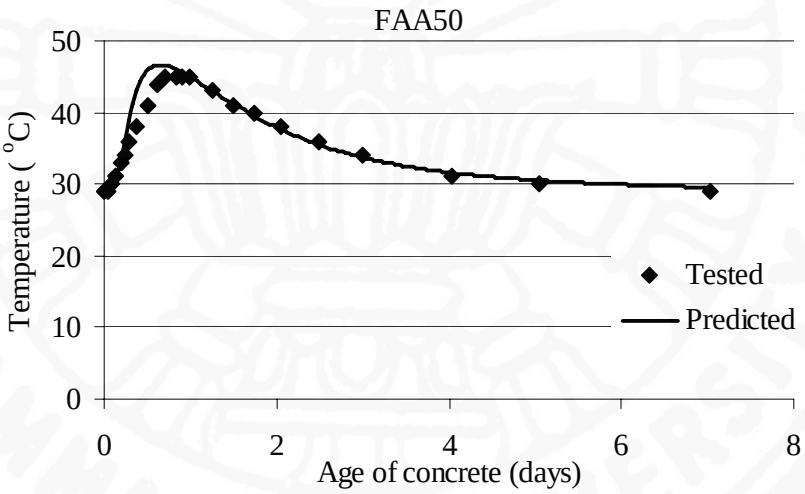

Fig. 8.11 Comparison between test and predicted temperature of blended cement mixture with 50% replacement of fly ash type A (FAA50)

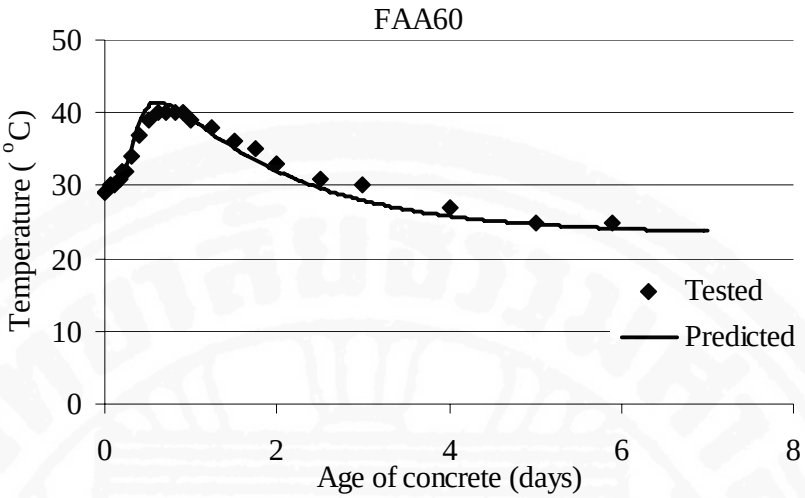

Fig. 8.12 Comparison between test and predicted temperature of blended cement mixture with 60% replacement of fly ash type A (FAA60)

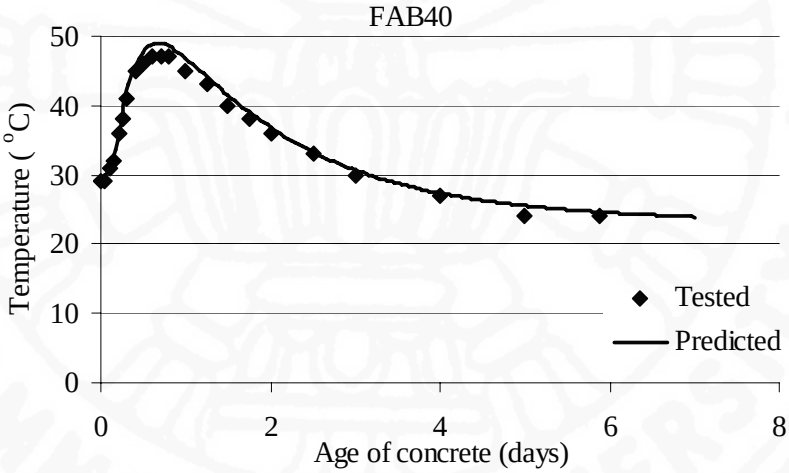

Fig. 8.13 Comparison between test and predicted temperature of blended cement mixture with 40% replacement of fly ash type B (FAB40)

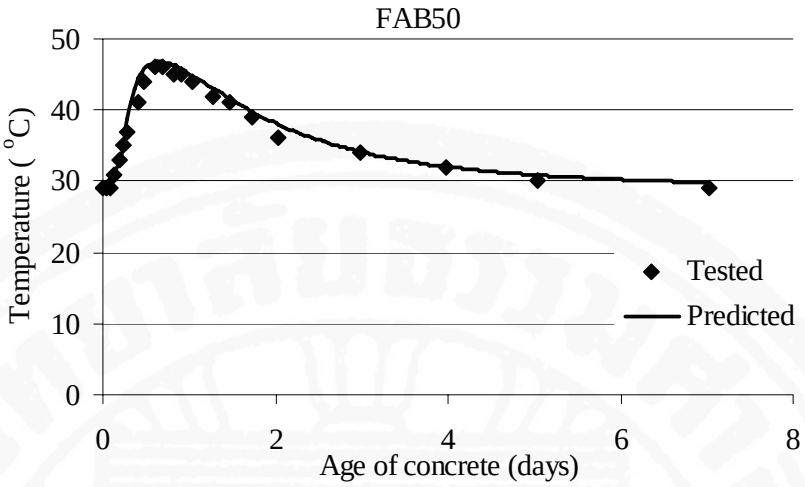

Fig. 8.14 Comparison between test and predicted temperature of blended cement mixture with 50% replacement of fly ash type B (FAB50)

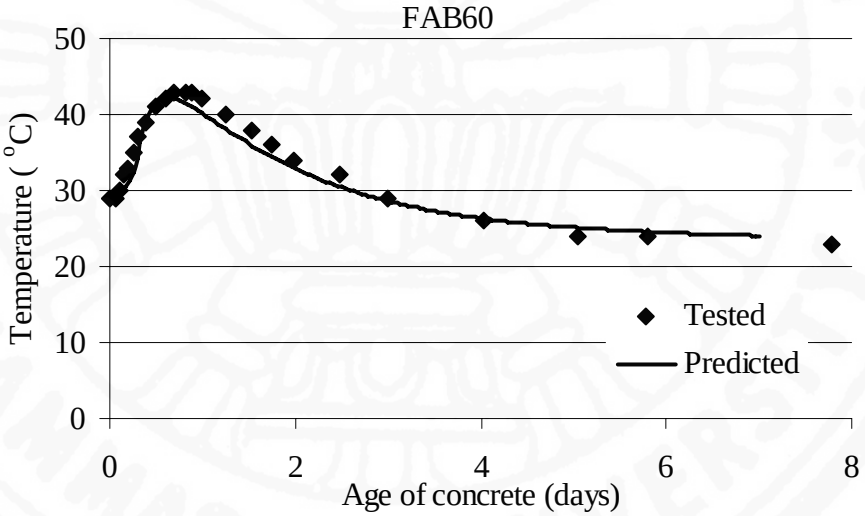

Fig. 8.15 Comparison between test and predicted temperature of blended cement mixture with 60% replacement of fly ash type B (FAB60)

8.3.2 Verification with the test results of the real mass concrete footings

The developed semi-adiabatic temperature model was applied to compute the temperature of various mass concrete footings of some construction projects in Bangkok. The footings were cast with various dimensions and fly ash replacement ratios (r) were between 0.35 and 0.5. The mix proportions of concrete used for each footing are shown in Appendix D (Table D5). Two brands of Ordinary Portland cement (OPC) and lignite fly ash from a single source were used as cementitious materials. Physical properties and chemical composition used in the analysis of cement and fly ash (FA1) are shown in Table D6 and D7, respectively. Due to the limitation of the environmental data, the heat loss to the surrounding was obtained

from back calculation. The measuring positions of footings F1 to F10 are shown in Fig. 8.16. Temperatures were measured at center part of footing with various depths (10-30 cm. from top and bottom and mid height of footing). Figs 8.17 to 8.26 show the comparisons between test and predicted temperature at top, center and bottom measured points of footings F1 to F10.

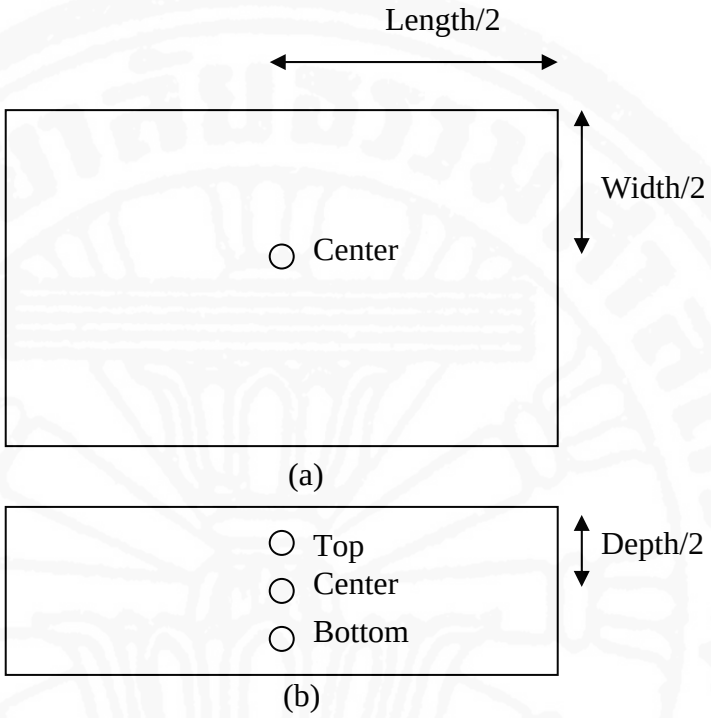

Fig 8.16 Temperature measuring positions of footings (a) top view, (b) side view

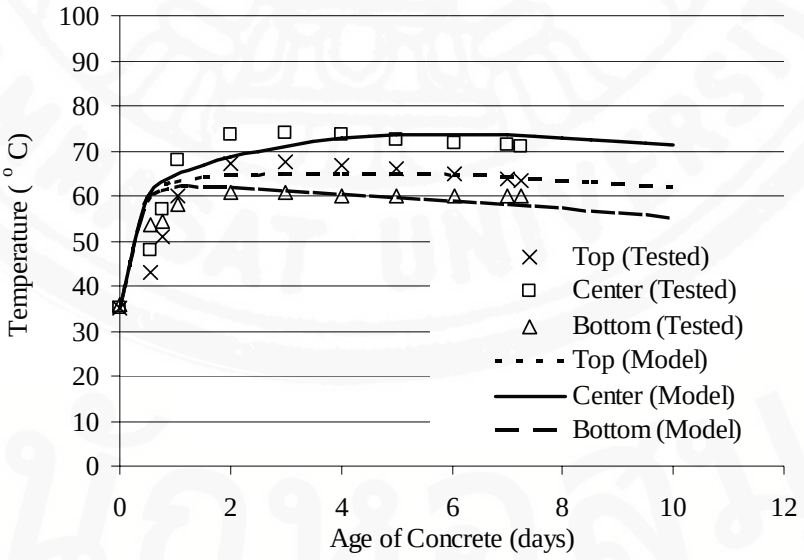

Fig 8.17 Comparison between test and predicted temperature at top, center and bottom of footing size 16.4x21.15x3 m. with 50 % fly ash replacement (F1).

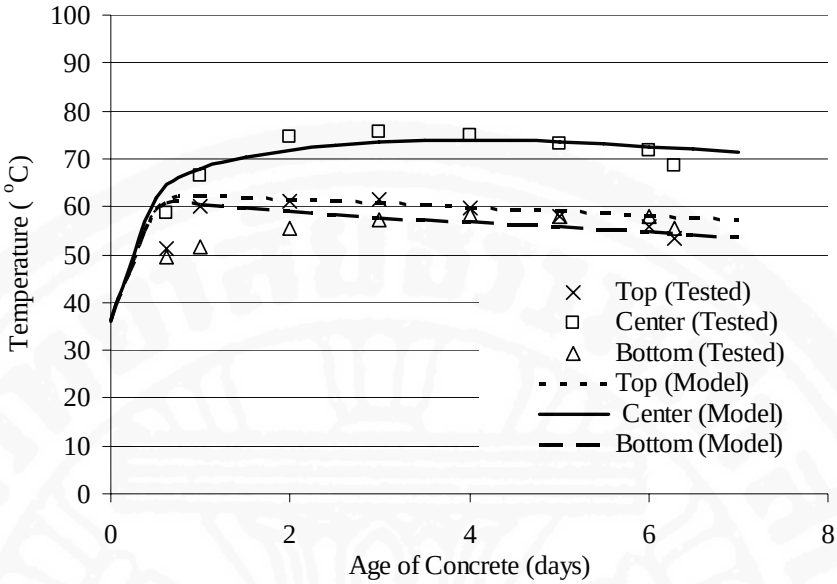

Fig 8.18. Comparison between test and predicted temperature at top, center and bottom of footing size 13.2x24.9x2.5 m. with 36 % fly ash replacement (F2)

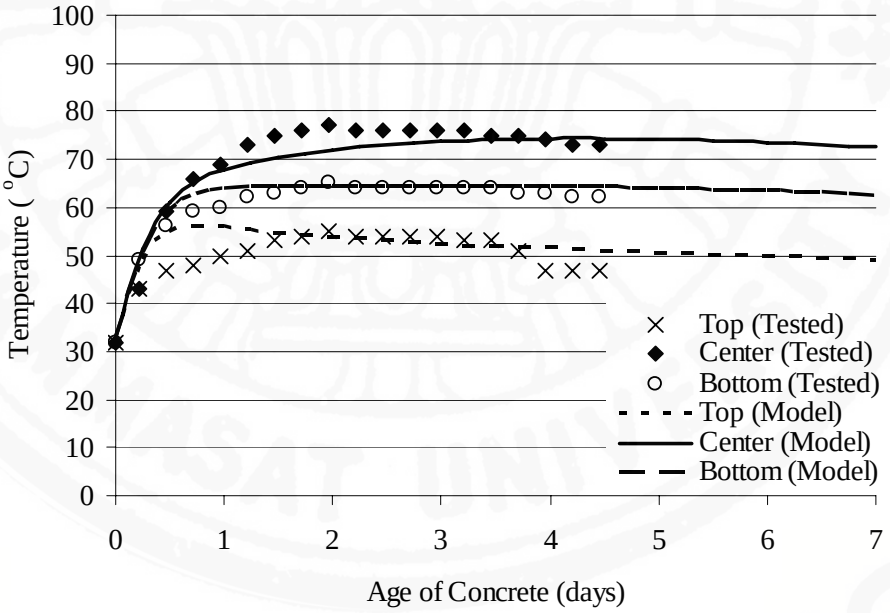

Fig 8.19 Comparison between test and predicted temperature at top, center and bottom of footing size 18.6 x 31 x 2.5 m with 35 % fly ash replacement (F3).

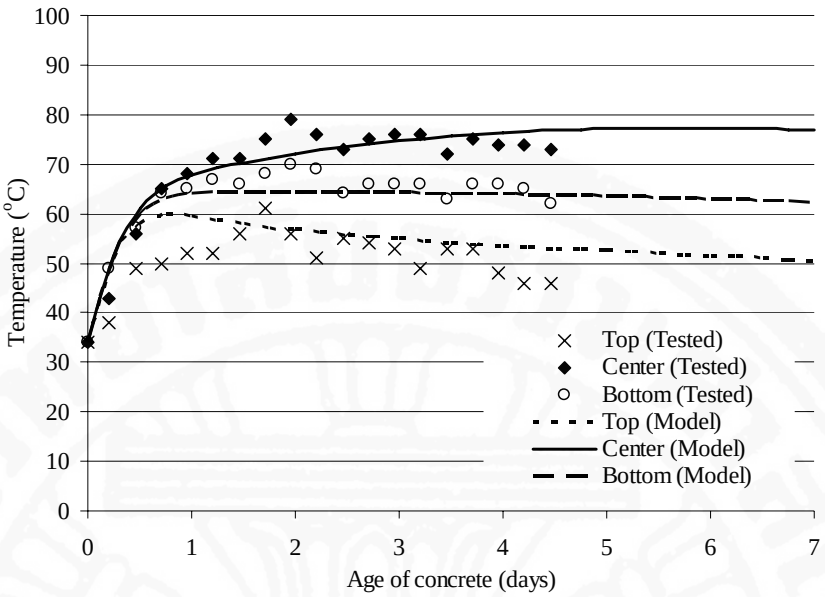

Fig. 8.20 Comparison between test and predicted temperature at top, center and bottom of footing size 14x17x3.5 m. with 35 % fly ash replacement (F4).

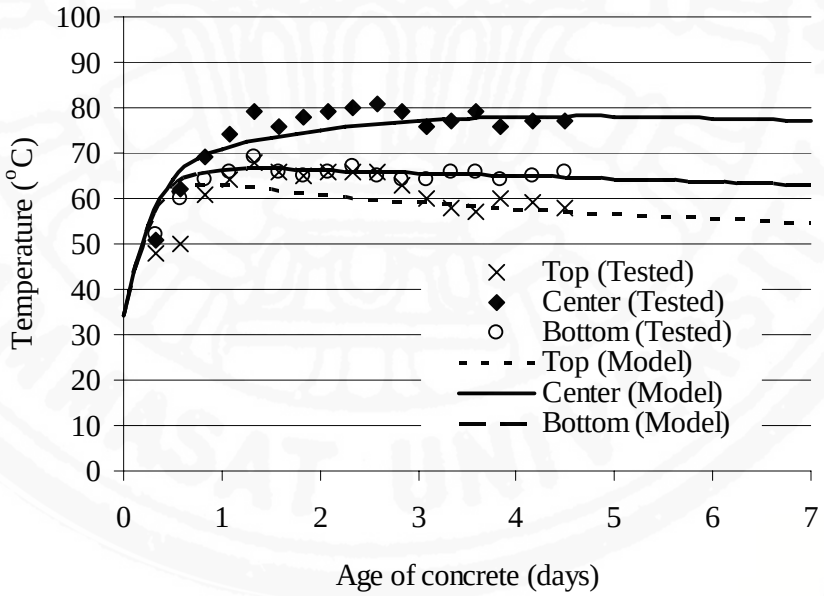

Fig. 8.21 Comparison between test and predicted temperature at top, center and bottom of footing size 23 x 26.8 x3 m. with 35 % fly ash replacement (F5).

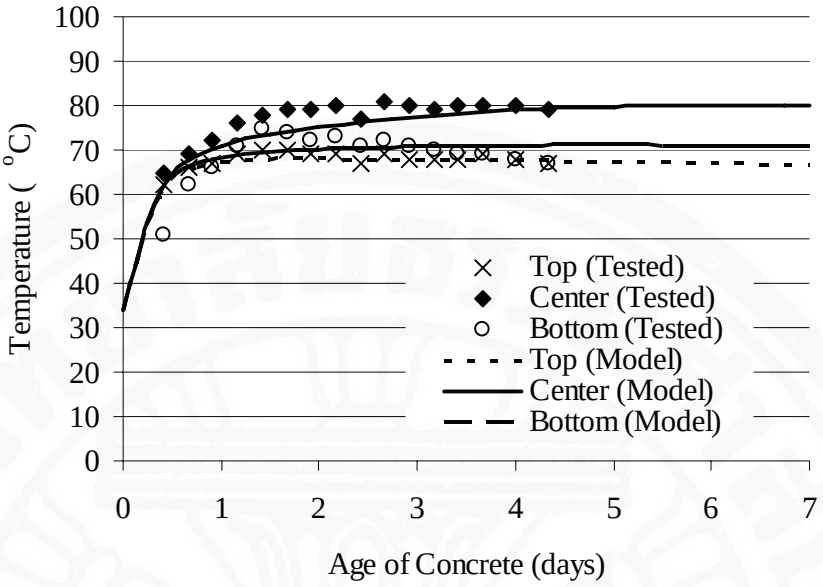

Fig. 8.22 Comparison between test and predicted temperature at top, center and bottom of footing, size 14x 26.8 x 3 m. with 35 % fly ash replacement (F6).

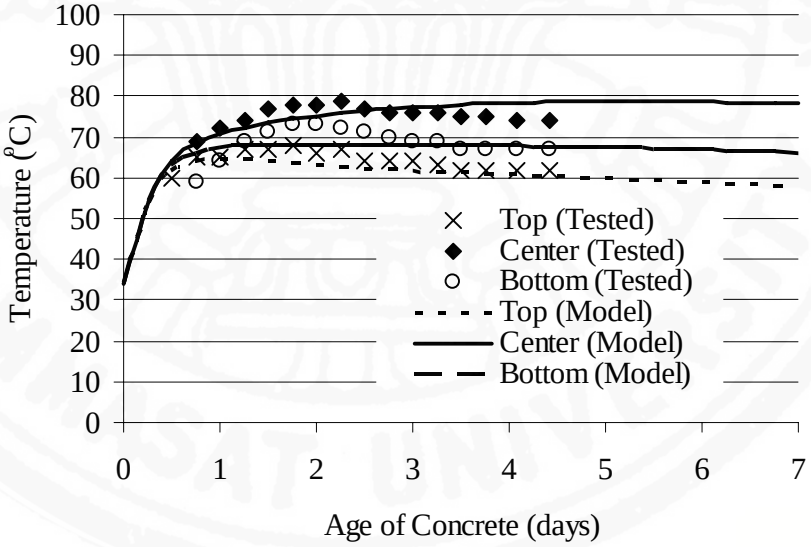

Fig. 8.23 Comparison between test and predicted temperature at top, center and bottom of footing size 13.6 x 26.8 x 3 m. with 35 % fly ash replacement (F7).

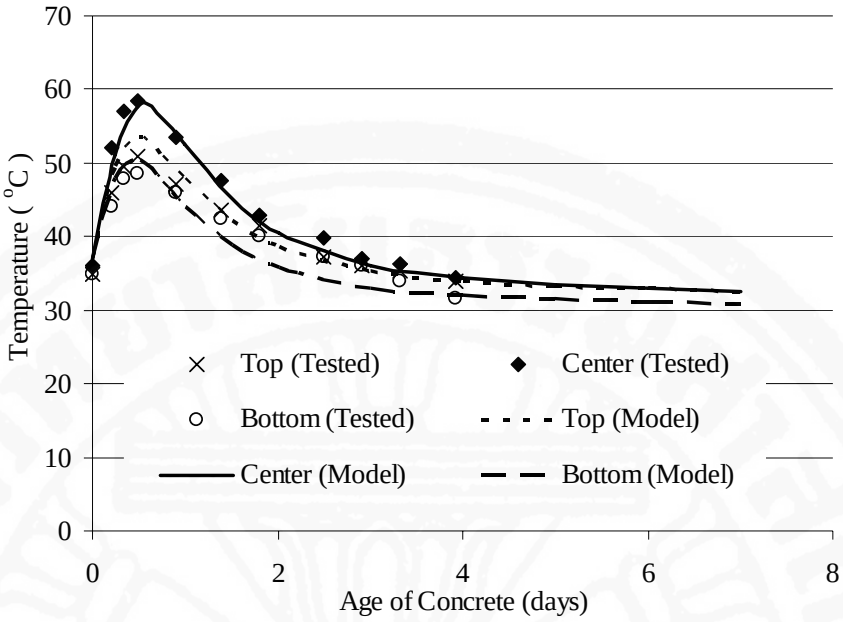

Fig. 8.24 Comparison between test and predicted temperature at top, center and bottom of footing size 1 x 1 x 1 m with 50 % fly ash replacement (F8).

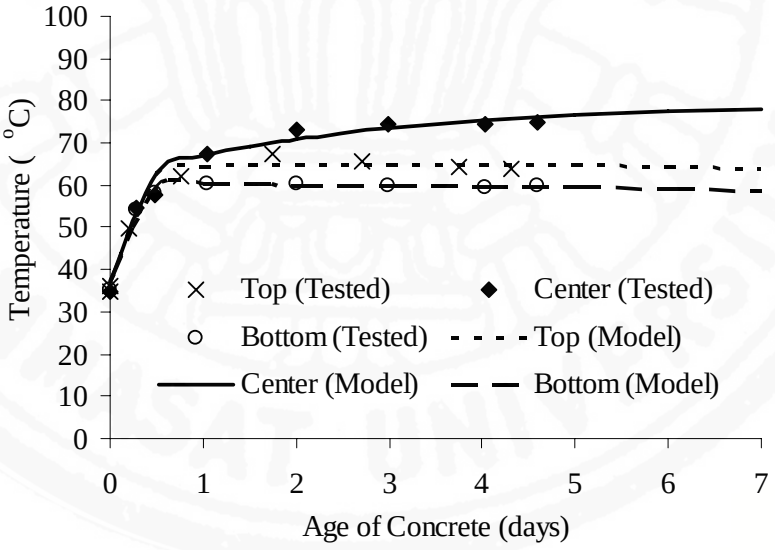

Fig. 8.25 Comparison between test and predicted temperature at top, center and bottom of footing size 17 x 19 x 3.5 m with 50 % fly ash replacement (F9).

The proposed computerized program was also verified with the test results of temperature measured at one side of a footing (footing number F11). The measuring positions are shown in Fig. 8.27. The measured temperatures of the footing was compared with the computed results as shown in Fig. 8.28.

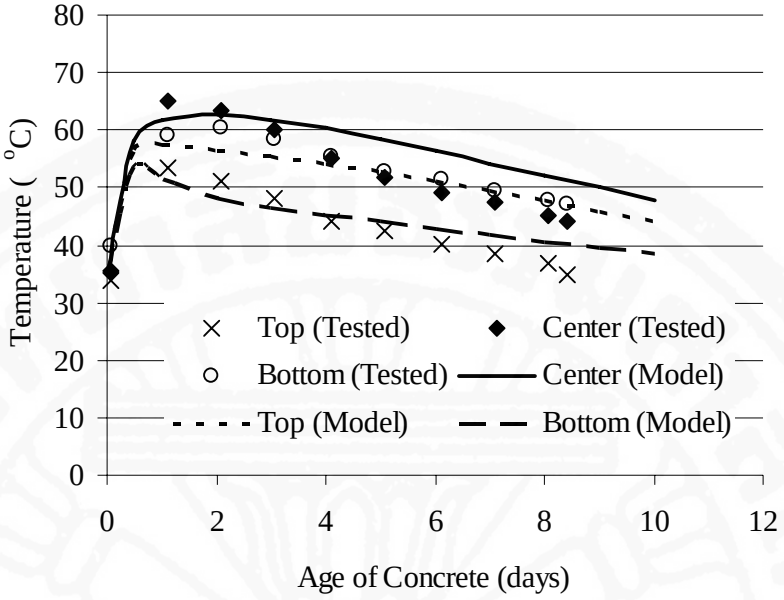

Fig. 8.26. Comparison between test and predicted temperature at top, center and bottom of footing size 25 x 40 x 1.8 m with 50 % fly ash replacement (F10).

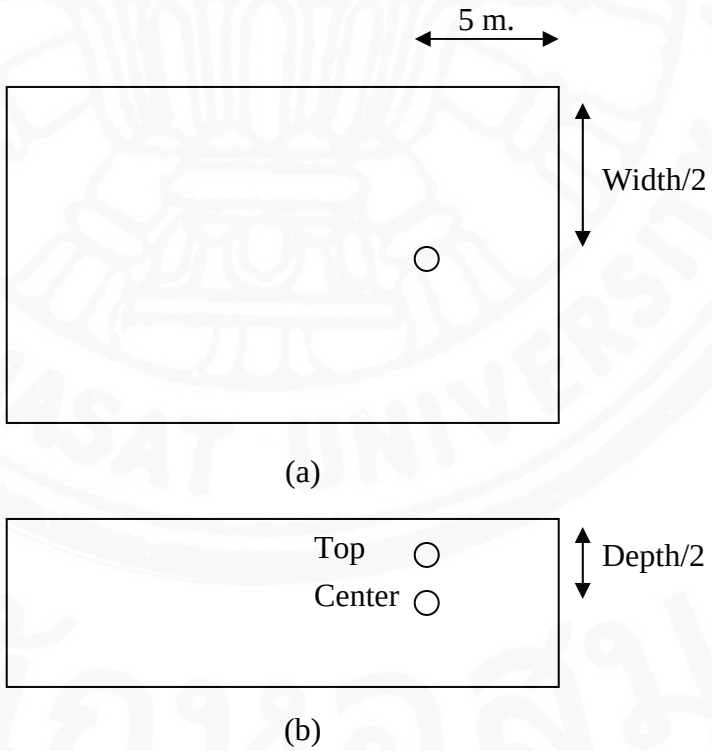

Fig 8.27 Temperature measuring positions of footings, F11, size 33x49.2x3 m, (a) top view, (b) side view

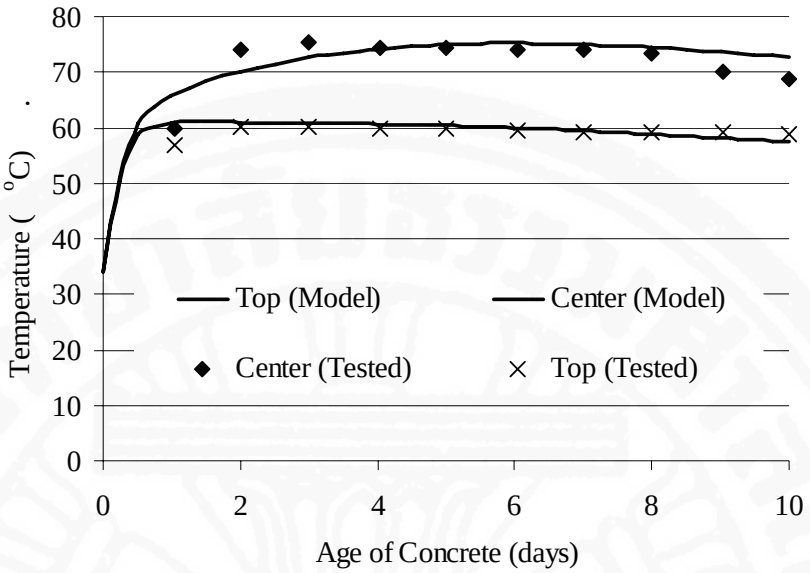

Fig. 8.28 Comparison between test and predicted temperature at center of footing, F11, size 33x49.2x3 m. with 50 % fly ash replacement

The developed computerized program was also applied to compute the temperature of a footing of the Elevated Railway Project in Bangkok (footing no. F12). The footing was cast with the dimensions of 38.4×8.4×4.75 m. and used a mix proportion with 47.5% of cement replaced by Mae-Moh fly ash (FA1 in Table D6 and D7). The temperature measuring positions are shown in Fig. 8.29. The measured temperatures at a corner and center part of footing were compared with the computed results as shown in Fig. 8.30 and 8.31.

The verifications of footings in all cases show that the proposed computerized program is satisfactory for predicting temperature of the mass concrete footings.

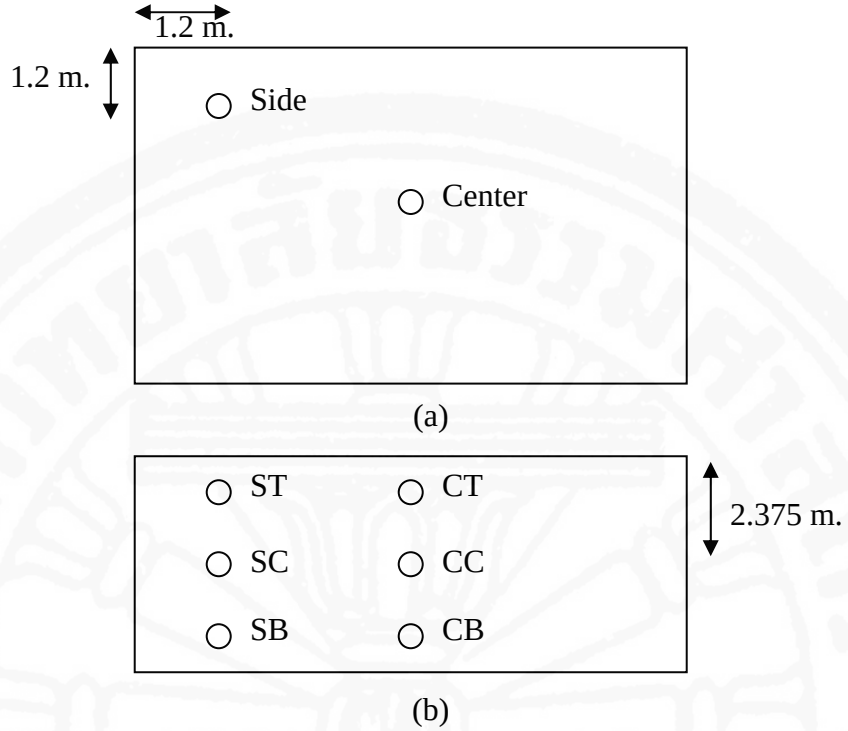

Fig 8.29 Temperature measuring positions of footing, F12, size 38.4x8.4x4.75 m. (a) top view, (b) side view

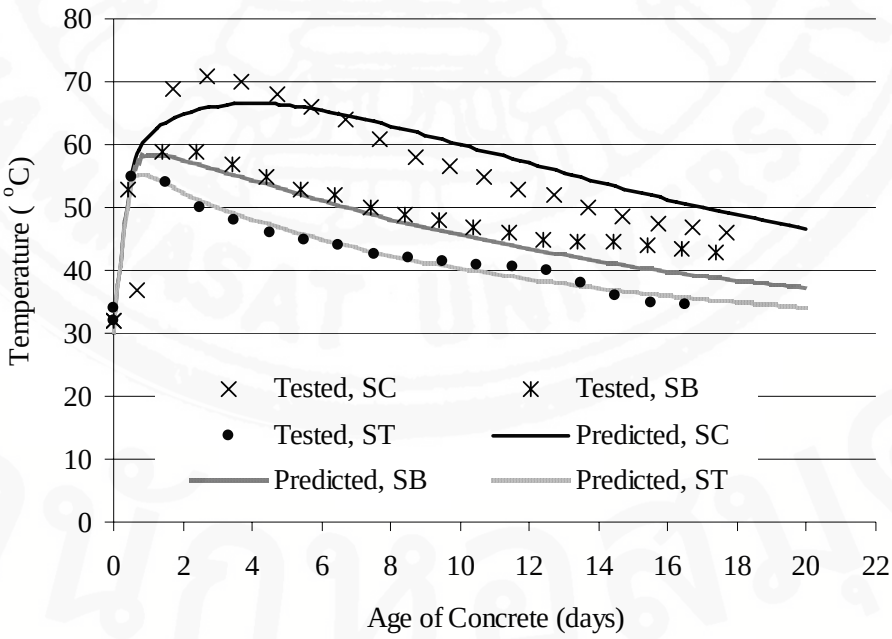

Fig 8.30 Comparison between test and predicted temperature at top, center and bottom of footing, F12, size 38.4x8.4x4.75 m. with 47.5 % fly ash replacement

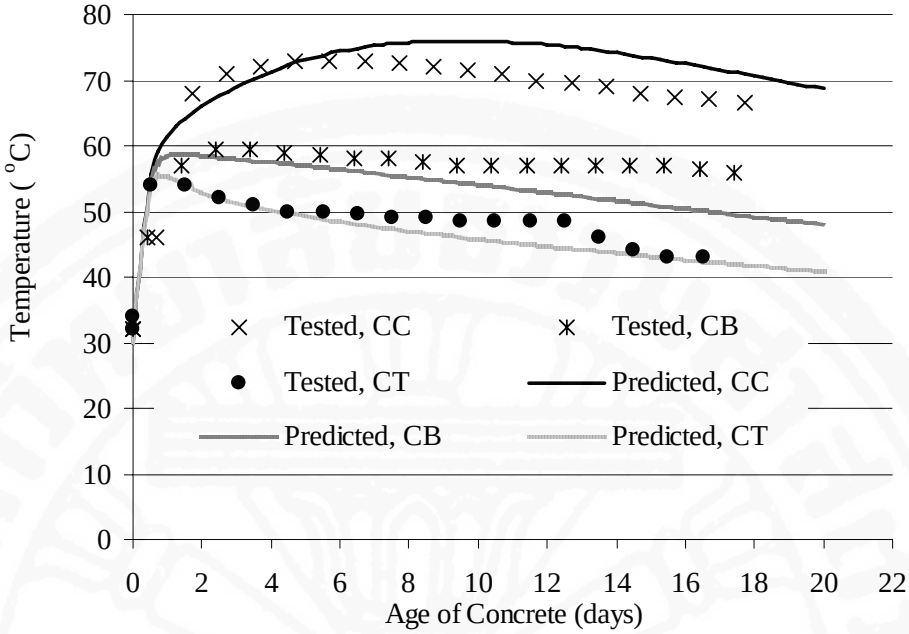

Fig. 8.31 Comparison between test and predicted temperature at top, center and bottom of footing, F12, size 38.4x8.4x4.75 m. with 47.5 % fly ash replacement

8.4 Restrained Strain Analysis

There are mainly two concepts that have been used to evaluate the risk of cracking in concrete. One applies the ultimate tensile strength and the other adopted the tensile strain capacity (TSC) concept. Both concepts can be used to evaluate the risk of cracking with acceptable result. However, Tongaroonsri and Tangtermsirikul (2008) found that based on the TSC rather than tensile strength, the prediction of the initiation of crack in concrete can be more accurately evaluated. Fig 8.32 shows an example of stress-strain relationship of concrete at tensile surface of a concrete prism specimen. The specimen was tested by using 3-point bending test. It was found that by using tensile strength concept, concrete is evaluated to crack at point A where the tensile stress first achieved maximum, however, at ultimate tensile stress, the strain at the tensile surface of concrete can still extend for a while and the first crack was found at point B. Many concrete samples cast using different mix proportion and materials show the similar behavior. As a result, by using the use of tensile strain capacity concept, the occurrence of crack can be more accurately predicted.

In each time step, the temperature at each position in mass concrete obtained from heat transfer analysis is used as the input for the restrained strain analysis. The internal deformation and stress in each element are related by Hooke's law as shown in Eq. (8.4).

The restrained strain is defined in Eq. (8.5). In case of absence of external loading, the stresses that cause cracking of early age concrete are induced by self-restraint deformations. The thermal strain of concrete element subject to temperature change can be calculated from Eq. (8.6). The effect of creep and shrinkage strain are not included in the analysis, then the difference between total strain and thermal strain becomes the restrained strain in concrete and

the stress-strain relation in Eq. (8.4) is transformed to be Eq. (8.7). The coefficient of thermal expansion (*CTE*) of concrete used in this study is obtained from Chapter 7.

$$\{\Delta\sigma(t)\} = E(t)\left[\overline{D}\right]\{\Delta\varepsilon_{res}(t)\} \tag{8.4}$$

$$\{\Delta\varepsilon_{res}(t)\} = \{\Delta\varepsilon_{T}(t)\} - (\{\Delta\varepsilon_{cr}(t)\} + \{\Delta\varepsilon_{sh}(t)\} + \{\Delta\varepsilon_{th}(t)\}) \tag{8.5}$$

$$\Delta\varepsilon_{th}(t) = CTE\ (t)\Delta T(t) \tag{8.6}$$

$$\{\Delta\sigma(t)\} = E(t)\left[\overline{D}\right](\{\Delta\varepsilon_{T}(t)\} - \{\Delta\varepsilon_{th}(t)\}) \tag{8.7}$$

where $\Delta\sigma(t)$ is the change of stress at the considered age (MPa), $\Delta\varepsilon_T(t)$, $\Delta\varepsilon_{res}(t)$, $\Delta\varepsilon_{cr}(t)$, $\Delta\varepsilon_{sh}(t)$ and $\Delta\varepsilon_{th}(t)$ are the changes of total strain, restrained strain, creep strain, shrinkage strain and thermal strain at the considered age, respectively (micron). CTE(t) is the coefficient of thermal expansion coefficient (micron/ ^{o}C) and $\Delta T(t)$ is the temperature change at the considered age (^{o}C). $E(t)$ is the modulus of elasticity at the considered age (MPa). $\left[\overline{D}\right]$ is the material properties matrix and t is the considered age.

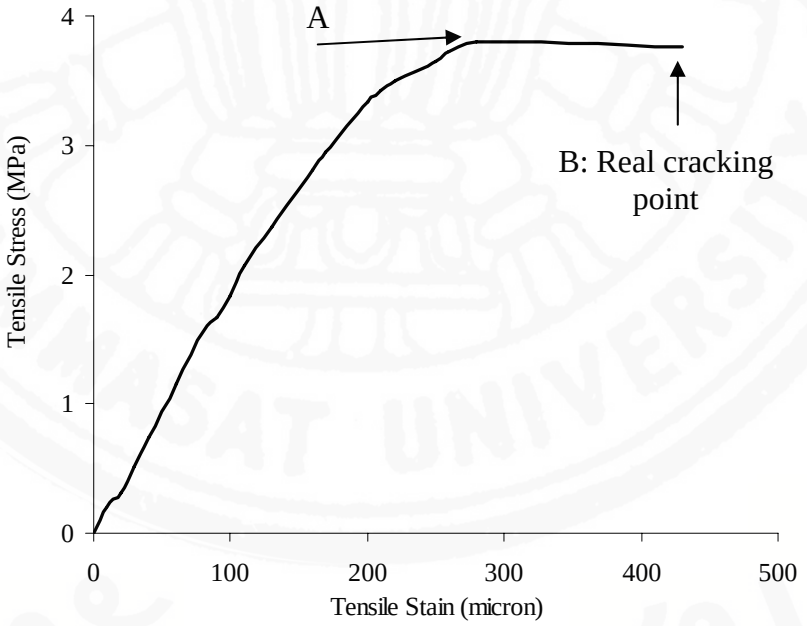

Fig. 8.32 Relationship between tensile stress and tensile strain on the tensile surface of a concrete beam specimen loaded by 3-point bending method

8.4.1 Example of the analytical results of restrained strain of mass concrete

A mass concrete footing "F11" was used as an example in the analysis. The restraint condition in this study was self-restraint. The effect of external restraint from the piles cap at bottom part of footing was included in the analysis. The results at the center part at various depths of the footing, as specified in Fig 8.33, are shown in Figs 8.33 to 8.37. The analytical results of temperature, free expansion thermal strain, actual strain, thermal stress, and restrained strain are shown in Figs 8.34, 8.35, 8.36, 8.37 and 8.38, respectively. When mass concrete is placed, there is a risk of thermal cracking due to temperature gradient within the concrete. Because thermal conductivity of concrete is low, heat can not easily transfer from center to surface, then temperature gradient occurs within the concrete because the interior portion becomes hot while the surface loses heat to the environment. The interior portion is thus restrained from free thermal expansion, so that compressive stress is induced and is balanced by the tensile stress near the surface, resulting in cracking at the surface due to self-restraint. From Fig 8.34, it was found that the highest temperature occurred at the center of the structure and the lowest was at the top surface.

The different expansion between center and surface also causes restraint between center and surface of structure. In case of free expansion (Fig. 8.35), the higher temperature part undergoes higher expansion than the lower temperature one, however, in reality the whole structure expands almost equally (the center part expands more than the top and bottom parts but the differences are small as shown in Fig 8.36). The surface was restrained by tensile stress while compression was at the center (Fig. 8.37). So, the surface is restrained in tension and center part is restrained in compression as shown in Fig 8.38. It was found from Figs. 8.34 to 8.38 that the analytical results show the same tendency as that occurs in mass concrete. In this study, the restrained strain is used to explain the potential of cracking in mass concrete. The restrained strain in tension ($\varepsilon_{res,\ ten}$) at point A is the highest then the results at point A are used to describe the cracking risk in this study. The $\varepsilon_{res,\ ten}$ at point A obtained from the analysis is compared with other researchers's results (Lu et al., 2001; Tongaroonsri and Tangtermsirikul, 2008) of tensile strain capacity of concrete (TSC) and if the $\varepsilon_{res,\ ten}$ is higher than TSC then the mass concrete structure is predicted crack. The TSC used in this study was obtained from other researchers. Lu et al. (2001) conducted the experiments and found that when restrained strain of concrete reaches 111 micron, concrete tends to crack. In other study, Tongaroonsri and Tangtermsirikul (2008) conducted the experiments for measuring TSC of many different mixtures of concrete at various ages. The experimental results obtained from their study were applied to evaluate thermal cracking in the analysis.

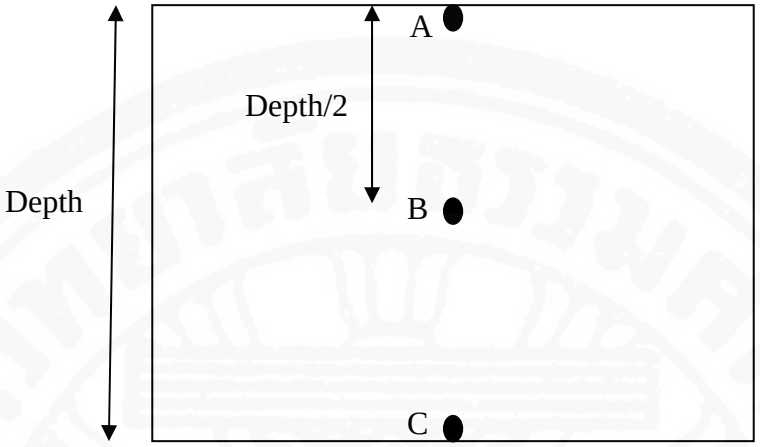

Fig. 8.33 Locations of temperature, thermal stress and restrained strain analysis (side view)

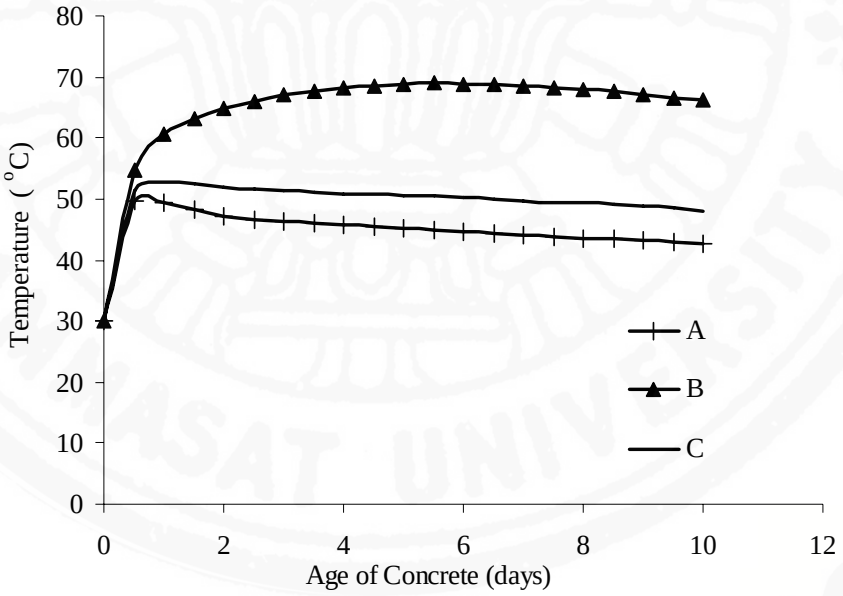

Fig. 8.34 Predicted temperature at top, center and bottom parts of a mass concrete

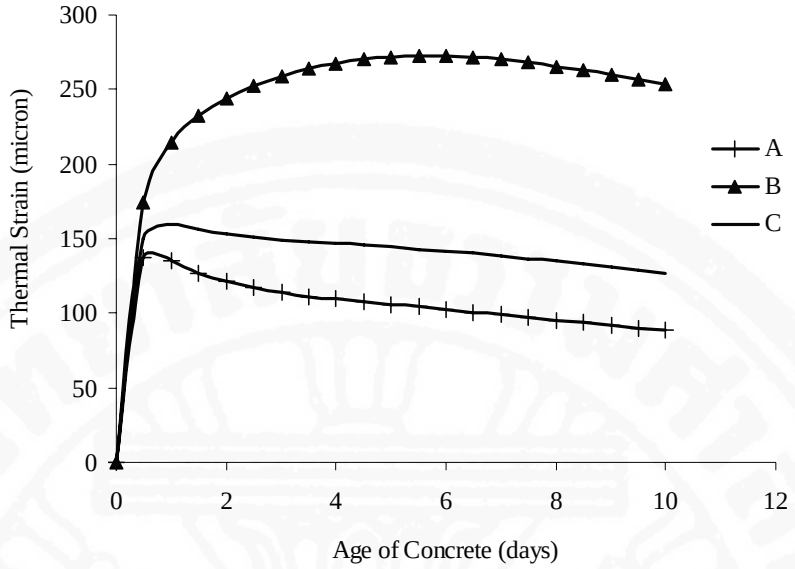

Fig. 8.35 Predicted free expansion thermal strain at top, center and bottom parts of a mass concrete

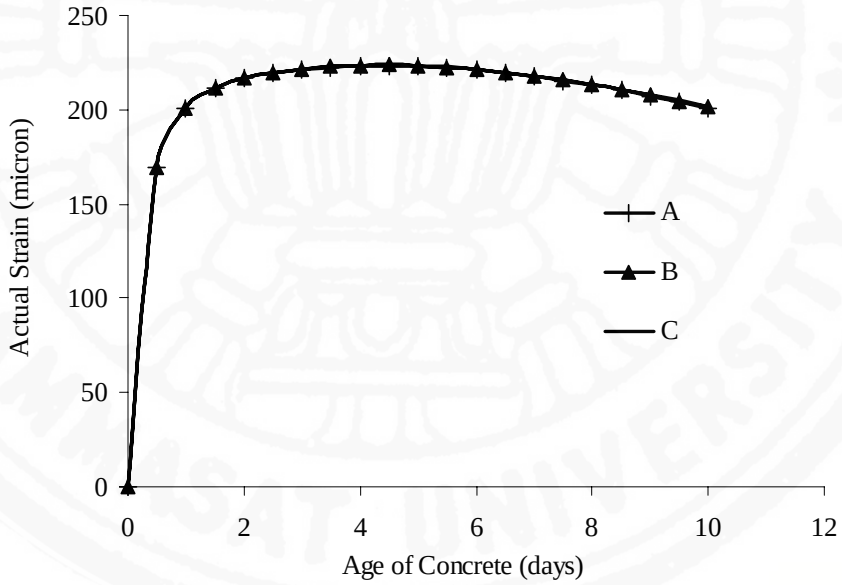

Fig. 8.36 Predicted actual strain at top, center and bottom parts of a mass concrete

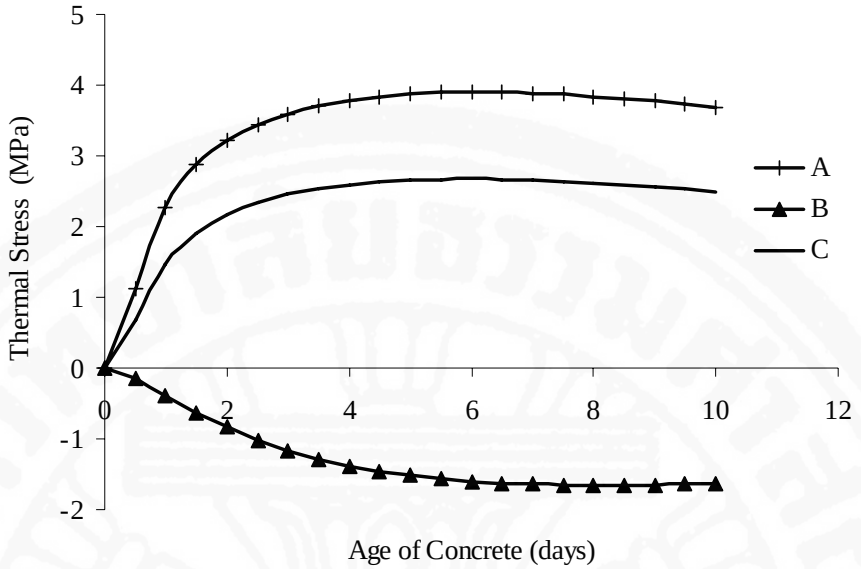

Fig. 8.37 Predicted thermal stress at top, center and bottom parts of a mass concrete

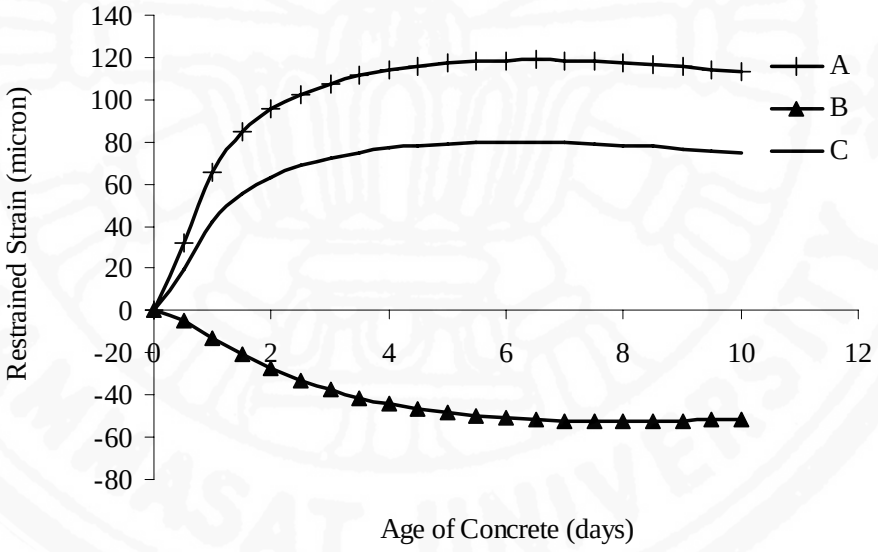

Fig. 8.38 Predicted restrained strain at top, center and bottom parts of a mass concrete

8.5 Verification of the Proposed Thermal Cracking Prediction Model with a Real Mass Concrete Footing.

The model was verified with a real concrete footing of a construction project in Bangkok, Thailand (footing F13 in Table D5). Figs 8.39 and 8.40 show a thermal crack at the top and side surfaces of the footing. The size of footing is 14 x 63 x 1.4 m. The mix proportion used for this footing is shown in Appendix D (Table D5). The footing was cured by insulated curing for 4.6 days. Cracks were found right after the removal of the insulation materials. This means that cracks might occur since early age before the removal of the insulation material.

The comparisons between measured and predicted temperature at 20 cm. from top surface, 20 cm. from bottom surface and at the center of the footing are shown in Fig 8.41. The analytical result of restrained strain at the core zone of top surface of footing was shown in Fig. 8.42. The rapid change of temperature and restrained strain on top surface after 4.6 days occurs due to the removal of insulation material. The verifications showed that the model is satisfactory for predicting temperature of the footing.

Fig 8.43 shows the comparisons between the predicted $\varepsilon_{res,\ ten}$ on top surface and TSC of concrete. By comparing the analyzed restrained strain with the test results of TSC conducted by Tongaroonsri and Tangtermsirikul (2008), the footing was predicted to crack since early age before the removal of the insulation material. The severity becomes higher after the insulation material was removed. The footing was predicted to have first crack after the removal of the insulation material when TSC of concrete proposed by Lu et al. (2001) was used in the comparison. It can be concluded that the model was satisfactory to predict thermal cracking of the footing.

Fig. 8.39 Crack on top surface of a footing

Fig. 8.40 Crack on side surface of a footing

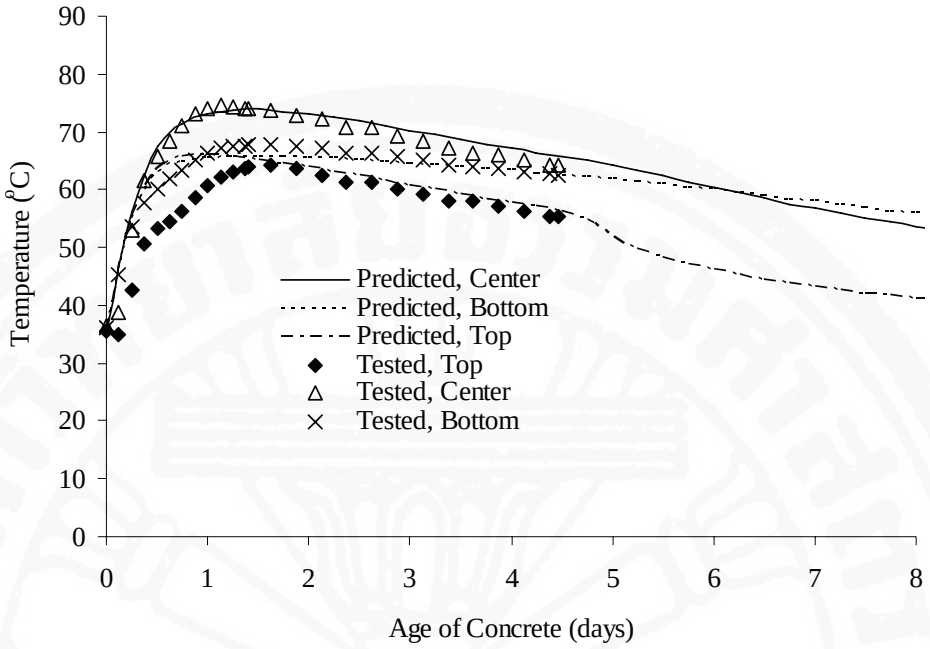

Fig. 8.41 Comparison between test and predicted temperature at top, center and bottom parts of a footing

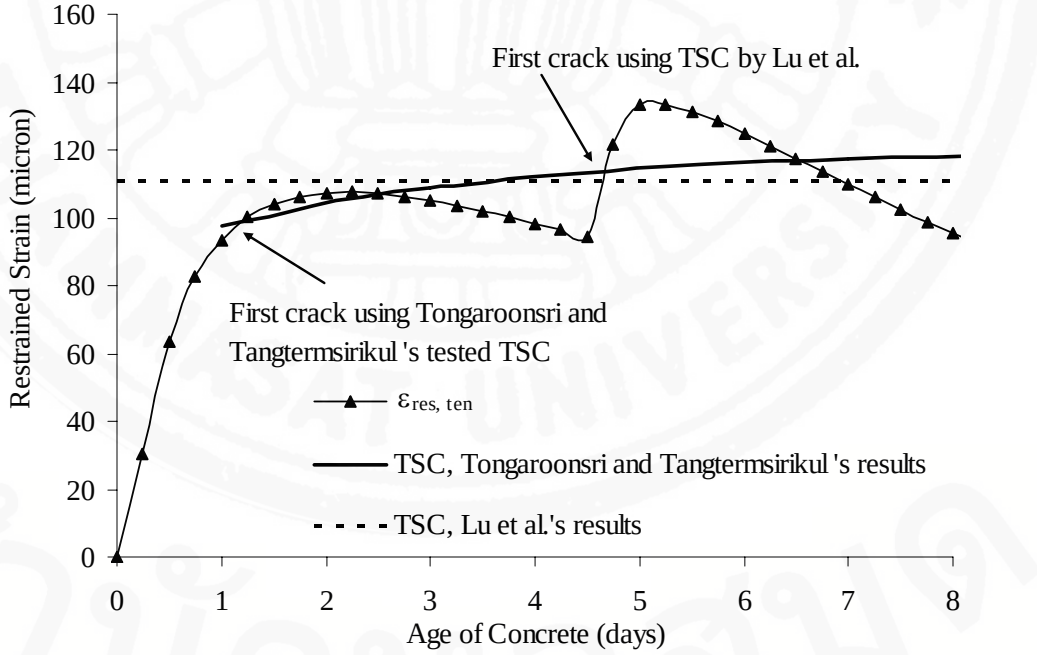

Fig. 8.42 Comparison between tensile strain capacity and predicted restrained strain of a footing